Computational Materials Science 199 (2021) 110724

Contents lists available at ScienceDirect

Computational Materials Science

journal homepage: www.elsevier.com/locate/commatsci

Multiphysics approaches for modeling nanostructural evolution during physical vapor deposition of phase-separating alloy films

Rahul Raghavan [a], William Farmer [a], Leslie T. Mushongera [b], Kumar Ankit [a,*]

[a] School for Engineering of Matter, Transport and Energy, Arizona State University, 551 E. Tyler Mall, Tempe, AZ 85287, USA
[b] Department of Chemical & Materials Engineering, University of Nevada, Reno 1664 N. Virginia Street, Reno, NV 89557, USA

A B S T R A C T

Physical vapor deposition of phase-separating alloy films yields a rich variety of distinct self-assembled nanostructures depending on the deposition rate and temperature. However, the role of grain boundaries, elastic imhomogeneity, and anisotropy, and surface tension, in the formation of such nanostructures is currently not well understood. Here, we employ a phase-field approach that couples the multiphysics of elemental diffusion, elastic misfit and anisotropy, surface tension, and grain boundaries with processing parameters, namely deposition rate and temperature, to investigate phase separation and grain boundary evolution in binary alloy films. We develop phase-field deposition models of increasing complexity to isolate and analyze the influence of processing parameters on nanostructural transitions in vapor co-deposited films. While it is found that such transitions are primarily guided by a minimization of total free energy, our simulation-based insights strongly indicate the phenomena of nanostructure selection at faster deposition rates. It is anticipated that the insights gained from this study will provide the much-required knowledgebase for establishing nanostructure-level control in the physical vapor deposition of alloy films.

1. Introduction

Nanostructural evolution during vapor-deposition of phase-separating alloy films is of considerable interest owing to their numerous functional properties that can be used in applications such as thin-film metallic glasses [1–3], nanoelectronic devices [4,5], and optoelectronic metamaterials [6,7]. Physical vapor deposition (PVD) is one of the techniques that enables the facile synthesis of such films. However, a classical challenge in this arena is the control of nanostructured morphologies that are extremely sensitive to processing parameters, such as the deposition rate, temperature, and film thickness. In particular, the precise mechanisms that govern nanostructural self-assembly in phase-separating alloy films have not been conclusively elucidated, as it continues to be a subject of conjecture. Therefore, numerical models that can simulate *in situ* phase separation during vapor co-deposition could help deduce the underlying mechanisms that govern the formation of characteristic nanoscaled morphologies in these films.

In PVD films, a combination of deposition conditions such as the rate (v), temperature, and composition can be varied to synthesize nanostructures that self-assemble into distinct patterns. For example, binary immiscible films of equimolar compositions are known to form distinguishable concentration modulations (CMs), such as vertical concentration modulations (VCMs), where the phases separate into layered domains [8–12], lateral concentration modulations (LCMs), where the domains appear as vertically oriented inter-penetrating shafts [13–18], or random CMs that lack any discernible self-assembly [19–21]. However, at non equimolar compositions, aligned rod (AR) morphology, where vertically aligned rods of the minority phase grow along the deposition direction in a matrix of the majority phase, have previously been observed [22–24].

Experimental studies that focus on phase-separated nanostructured films have their limits as far as deriving processing-nanostructure relationships is concerned. Transmission Electron Microscopy (TEM) of phase-separating immiscible alloy films [25–28,21] have shown transition from VCM to LCM morphologies with changes in deposition rate and temperature. However, a deeper understanding of the mechanisms that cause such transitions warrants extensive parametric studies, that may not be possible to attain using experimental techniques alone. Numerical models are inherently much faster and are, therefore a more viable alternative. In the past, numerous studies have attempted to correlate the film morphology with the relevant processing parameters [29–32]. Early studies by Atzmon et al. [33] and Adams et al. [34] suggested that phase separation during film growth is influenced by kinetic parameters, such as deposition rate and adatom mobility. The role of interfacial energy in inducing morphological transitions from LCM to VCM is also reported in these previous works. However, the frozen bulk approach used to formulate the deposition models in both the above-cited works restrict any phase separation to the film's surface.

* Corresponding author.
E-mail address: kumar.ankit@asu.edu (K. Ankit).

https://doi.org/10.1016/j.commatsci.2021.110724
Received 1 April 2021; Received in revised form 11 July 2021; Accepted 12 July 2021
Available online 23 July 2021

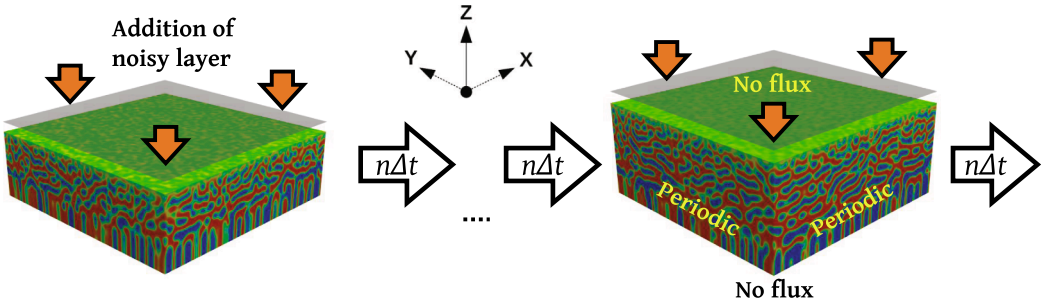

Fig. 1. Schematic diagram illustrating the technique adopted to simulate physical vapor deposition using the *preliminary* model. Here, Δt is the simulation timestep, whereas n denotes the number of iterations elapsed prior to addition of a new layer.

This approximation, therefore, overlooks the important physics of domain evolution below the film surface which may be prevalent in deposition experiments performed at higher temperatures or during post-deposition annealing. Lu et al. [35], using 2-D phase-field simulations, explored the role of composition and deposition rate on the evolution of phase separating domains in PVD films. Their study suggested that LCM to VCM transitions occur due to a change in the underlying mechanisms from templated growth to uphill diffusion. 3-D studies conducted by Ankit et al. [21] further explored the influence of mobility, in addition to deposition rate, and showed novel morphologies and transients such as mixed and random concentration modulations, which were overlooked in the 2-D studies. More recently, 3-D phase-field studies on vapor deposition of immiscible alloy films of non-equimolar compositions revealed the possibility of other variants, such as perforated-VCMs and globular morphologies [24]. The former is a layered morphology where the minority phase exists as perforated layers alternating with the majority phase, while the latter exhibits globules of the minority phase in a matrix of the majority phase. A recent study by Raghavan et al. [36] studied self-assembled surface protuberances evolving from patterned and randomly formed seed layers in phase-separated films. However, a common drawback in all of the models discussed thus far lies in their simplicity i.e. these models while making several assumptions ignore the multiphysics of lattice misfit, presence of grain boundaries, and surface grooving, and their impact on phase separation. In a more realistic deposition process, material properties such as elastic misfit, grain size, and orientation relationships, as well as associated phenomena of surface grooving and protuberance formations add further complexities that are non-trivial to comprehend. It is, therefore, imperative to formulate novel numerical models that can account for multiphysics associated with nanostructural evolution during PVD of phase-separating alloy films.

To fill this missing gap in past modeling efforts, here we report phase-field models that encapsulate the physics of elastic anisotropy and lattice misfit, grain boundaries and grain sizes, and surface energy, on the morphological evolution of nanostructured PVD films. We begin by leveraging the model developed by Ankit et al. [21,24], henceforth referred to as the *preliminary model*, to simulate nanostructural evolution during PVD of a single crystal binary phase-separating alloy film where the interfaces between nanosized-domains are assumed to be incoherent, while the dihedral angle between the surface and the vapor phase equals 180°. Next, we incorporate the contribution of elastic misfit energy into this model via a numerical scheme developed by Mushongera et al. [37,38] and evaluate the role of misfit strains and elastic anisotropy on the film's nanostructure. Following this, we expand the preliminary model to account for grain boundaries to simulate phase separation in a polycrystalline film and explore the implications of grain size on previously-reported LCM and VCM nanostructures. Finally, we explore the role of surface grooving and curvature on phase separation during PVD by proposing a ternary regular solution model where the concentration of the vapor phase, ϕ_v, is assumed to be the third order-parameter in addition to the other two, namely ϕ_A and ϕ_B, that represent co-depositing elements.

2. Methods

2.1. Preliminary model

Our numerical approach builds incrementally from a Cahn–Hilliard model for simulating phase separation in a binary single crystal alloy with no elastic misfit. In this preliminary model, the role of surface tension that can lead to the formation of surface grooves and protuberances is ignored. With this assumption, the free energy functional that consists of distinct bulk and interfacial energy terms [39], can be written as

$$F = \int_{\Omega} \left[f(\phi) + \frac{1}{2}\kappa |\nabla \phi|^2 \right] d\Omega, \tag{1}$$

where, the order parameter, $\phi(x,t)$, denotes the scaled concentration, which is dependent on both time and position, such that it varies from 0.0 in the B-rich β phase to 1.0 at the A-rich α phase [21,24]. For the bulk energy term, we employ a double-well formalism, which is commonly used for modeling the morphological evolution in spinodally decomposing alloys, given by

$$f(\phi) = \frac{1}{4} W \phi^2 (1-\phi)^2 \tag{2}$$

where, W is the well height which energetically favors states corresponding to $\phi = 0.0$ or 1.0, while κ is the gradient free energy coefficient that penalizes large gradients in ϕ giving rise to the diffuse interfaces. The morphological evolution of phase separating domains can then be simulated by solving the equation,

$$\frac{\partial \phi}{\partial t} = \nabla \cdot M \nabla \mu \tag{3}$$

where, μ is the chemical potential given by the variational derivative of the free energy functional as $\mu = \frac{\delta F}{\delta \phi}$, while M is the mobility of the diffusing elements which is related to the diffusion coefficient via $D = M \frac{\partial^2 f}{\partial \phi^2}$. In this *preliminary* model, we assume the kinetic parameter to be independent of the order parameter. Thus, the evolution equation may be rewritten as,

$$\frac{\partial \phi}{\partial t} = M \nabla^2 \frac{\delta F}{\delta \phi}. \tag{4}$$

Using Eqs. (1) and (2), we arrive at the final form of the Cahn–Hilliard equation,

$$\frac{\partial \phi}{\partial t} = M \nabla^2 \left[\frac{1}{2} W (2\phi^3 - 3\phi^2 + \phi) - \kappa \nabla^2 \phi \right]. \tag{5}$$

We simulate the temporal evolution of ϕ by co-depositing new layers of A and B starting from a non-decomposed seed of thickness, 20 grid-

Table 1
Simulation parameters used for phase-field modeling of nanostructural evolution during PVD of phase-separating binary alloy films.

Model Parameters	Preliminary Model	Misfit Model	Polycrystal Model	Vapor Phase Model
Free energy potential	$W = 4.0$	$W = 4.0$	$W = 4.0$	$\chi_{Av} = \chi_{Bv} =$ 2.7, 2.8 & 3.5 $\chi_{AB} = 3.5$
Gradient parameters	$\kappa_\phi = 2.0$	$\kappa_\phi = 2.0$	$\kappa_\phi = 2.0$, $\kappa_\eta = 1.0$	$\kappa_{AA} = \kappa_{BB} = 4.0$ $\kappa_{AB} = 3.0$
Kinetic parameters	$M = 0.1, 0.2, 0.3, 0.4, 0.5$	$M = 0.3$	$M_b/M_{gb} = 0.005, 0.06$	$D_A = D_B = 1.2$
Simulation Parameters				
$\Delta x = \Delta y$ (= Δz)	1.0	1.0	1.0	1.0
Δt	0.015–0.025	0.01	0.01	0.002
$N_x \times N_y \times (N_z)$	$300 \times 300 \times (300)$	300×300	200×200	$150 \times 150 \times (200)$

points ($20\Delta z$), in which the local composition fluctuates about the alloy composition via a Langevin noise term. For simplicity, the substrate is assumed to be non-reactive. The simulation domain comprises 300×300 grid-points along the x and y directions, while new layers are co-deposited in the z-direction until the film's thickness reaches 300 grid points. The deposition rate, υ, is a dimensionless quantity that is adjusted by depositing a layer of thickness Δz after every $n\Delta t$ time interval, where n denotes the number of iterations elapsed before addition of a new layer (Fig. 1). A fresh layer (with composition fluctuations) of thickness Δz is deposited at a frequency of $n\Delta t$, where n denotes the number of simulation timesteps in between deposition of layers (Fig. 1). Thus, the dimensionless deposition rate is given by $\upsilon = \frac{1}{n\Delta t}$. M and υ are varied from 0.1 to 0.5 and 0.05 to 0.4, respectively, to explore the role of both these kinetic parameters on the nanostructural evolution. A detailed account of numerical techniques adopted to solve Eq. (5) is available in our previous works [21,24]. All the relevant simulation parameters are listed in Table 1.

2.2. Incorporating lattice misfit

Phase separation during PVD can induce elastic stresses in the film that may have a dominant effect on the nanostructural evolution. The evolving nanostructured interfaces can be expected to possess lattice misfit energies, while the film itself can be elastically non-–homogeneous. In the present model, these effects can be incorporated via a ϕ-dependent elastic energy density term, $E_{el}(\phi)$, which is added to the total free energy density,

$$F = \int_\Omega \left[f(\phi) + \frac{1}{2}\kappa|\nabla\phi|^2 + E_{el}(\phi) \right] d\Omega. \tag{6}$$

A stress-free strain or eigenstrain tensor, ϵ^0_{ik}, is employed to define the elastic energy density, written as

$$E_{el}(\phi) = \frac{1}{2}\sum_{iklm}(\epsilon_{ik} - \overrightarrow{\epsilon}^0_{ik}) C_{iklm} (\epsilon_{lm} - \overrightarrow{\epsilon}^0_{lm}), \tag{7}$$

where $\overrightarrow{C}_{iklm}$, the stiffness tensor. The elastic constants of the alloying components are assumed to be distinct, thereby rendering the system elastically inhomogeneous and anisotropic. These are then coupled to the ϕ-dependent elastic moduli for the film via an interpolation function, $h(\phi)$ which assumes a value $h(\phi) = \phi^2(3-2\phi)$ [40]. This equation is

Table 2
Elastic constants used to simulate nanostructural evolution during PVD of phase-separating binary alloy films.

Elastic Constants ($\times 10^{10}$ J/m^3)	A	B
Case 1: Elastically homogeneous film		
C_{11}	30.0	30.0
C_{12}	16.0	16.0
C_{44}	7.0	7.0
Case 2: Elastic anisotropy in film due to bulk modulus (ξ^α_K, ξ^β_K = 0.44, 2.80)		
C_{11}	48.0	21.0
C_{12}	16.0	16.0
C_{44}	7.0	7.0
Case 3: Elastic anisotropy in film due to shear modulus (ξ_s = 2.66)		
C_{11}	30.0	30.0
C_{12}	16.0	16.0
C_{44}	16.0	6.0
Eigenstrain, ϵ_{ik}	−0.15 %	

written as,

$$C_{iklm}(\phi) = C^\alpha_{iklm} h(\phi) + C^\beta_{iklm}(1 - h(\phi)), \tag{8}$$

where C^α_{iklm} and C^β_{iklm} are the elastic constants of the corresponding pure α and β phases. The stiffness tensor, C_{iklm}, is symmetric under the interchange of i,k for l,m and of i,m for k,l, and has symmetries reflecting those of the crystalline lattice. The eigenstrain is also coupled to ϕ by defining the B-rich β phase as the reference phase, such that its eigenstrain vanishes, yielding

$$\overrightarrow{\epsilon}^0_{ik}(\phi) = (1 - h(\phi))\epsilon^0_{ik}, \tag{9}$$

where $\overrightarrow{\epsilon}^0_{ik}$ represents coefficients of the strain tensor which is determined by the crystallography of the phases. The eigenstrain is defined as

$$\epsilon^0_{ik} = 2\left(\frac{a^\alpha - a^\beta}{a^\alpha + a^\beta}\right)\delta_{ik}, \tag{10}$$

where a^α and a^β are lattice parameters of the two phases, and δ_{ik} is the Kronecker-delta function.

In a purely elastic framework, mechanical equilibrium in a coherent phase-separated alloy film is achieved when the cumulative elastic stresses across the film equate to zero, such that

$$\sum_k \frac{\partial \sigma_{ik}(\phi)}{\partial x_k} = 0, \tag{11}$$

where the stresses are given by $\sigma_{ik}(\phi) = \partial E_{el}(\phi)/\partial\epsilon_{ik}$. The system of equations described by Eq. (6)–(11) is equilibriated five times per phase-field time-step (Eq. (3)). This assumption is justified given that the elastic state of a material, which changes with the speed of sound, is faster than atomic diffusion.

To assess the effect of elastic anisotropy during phase separation, we define the parameter, ξ_K, which measures the degree of anisotropy due to bulk modulus, as

$$\xi^i_K = \frac{2\{C_{44}\}^i}{\{C_{11}\}^i - \{C_{12}\}^i}, \tag{12}$$

where, C_{11},C_{12}, and C_{44} are elastic constants and $i \in \{\alpha,\beta\}$, depending on the phase that is being considered. $\xi_K > 1$ signifies that the corresponding phase has a positive elastic anisotropy due to bulk contributions, while $\xi_K < 1$ signifies a negative contribution.

The degree of anisotropy due to shear modulus of the component phases, ξ_s is defined as,

$$\xi_s = \frac{\{C_{44}\}^{\alpha}}{\{C_{44}\}^{\beta}}. \tag{13}$$

In the following study, we evaluate phase separation in films with zero elastic anisotropy, and with elastic anisotropy due to the bulk modulus and shear modulus, respectively. The principal elastic moduli and misfit eigenstrain imposed on the film in the three cases are listed in Table 2. For simulations, we use a domain of size 300 × 300 grid points along the x and z directions. The specifics of the deposition model are identical to the *preliminary* model, with the exception that the films are simulated in 2-D to simplify the analysis of elastic effects on the evolving nanostructure. The corresponding modeling parameters are summarized in Table 1.

2.3. Incorporating grain boundaries

The effect of grain boundaries on evolution and coarsening of phase-separated domains is studied by building a deposition model that demarcates the grains in a bicrystal film via an additional phase-field parameter, η. The revised free energy functional for modeling the evolution of phase separate domains in a polycrystalline film can be written as

$$F = \int_V [f(\phi, \eta_i) + \kappa_\phi |\nabla \phi|^2 + \sum_i^n \kappa_\eta |\nabla \eta_i|^2] dV, \tag{14}$$

where, the bulk free energy density also depends on the non-conserved order parameter, η, in addition to scaled concentration, ϕ, which is conserved. Additionally, the overall interfacial energy density is composed of η-dependent grain boundary, as well as the ϕ-dependent interfacial energy densities. The bulk free energy density in Eq. (14), which is based on a formulation for describing phase separation in polycrystalline materials by Ramanarayan et al. [41], is given by

$$f(\phi, \eta_i) = f(\phi) + m(\phi)\left\{0.25 + \sum_i^q \left[-\frac{\eta_i^2}{2} + \frac{\eta_i^4}{4}\right] + w_\epsilon \sum_i \sum_{j>i} \eta_i \eta_j\right\} \tag{15}$$

where $f(\phi)$ is the free energy of a single crystal of composition, ϕ assumed to be a double-well potential, as specified by Eq. (2), while the second term incorporates the contribution of non-conserved parameters, η_i, such that $f(\phi, \eta_i) = 0$ at $2q$ degenerate minima. w_ϵ is a constant and $m(\phi)$ is a composition-dependent function given by

$$m(\phi) = 1 + 0.1\phi^2 - 2\phi^2(1-\phi)^2. \tag{16}$$

Based on variational principles, the kinetic equations for ϕ and η can be written as

$$\frac{\partial \phi}{\partial t} = \nabla \cdot M(\eta_i) \nabla \frac{\delta F}{\delta \rho}, \text{ and} \tag{17}$$

$$\frac{\partial \eta_i}{\partial t} = -L\frac{\delta F}{\delta \eta_i} = -L\left[\frac{\partial f(\rho, \eta_i)}{\partial \eta_i} - 2\kappa_\eta \nabla^2 \eta_i\right], \tag{18}$$

where, the η-dependent atomic mobility [42] is given by,

$$M(\eta_i) = M_b + 4M_{gb}\left[\sum_{i,j>i} \eta_i^2 \eta_j^2\right]^{1/2}, \tag{19}$$

such that M_b represents the constant atomic mobility within the grain, whereas M_{gb} is a distinct pre-factor that controls atomic mobility within the grain boundaries. In Eq. (18), L is a relaxation parameter that controls the dynamics of grain boundaries.

Using Eqs. (17) and (18), we model PVD of an alloy film with grain boundaries that are vertically oriented along the deposition axis (z). Periodic boundary conditions are imposed along the edges that are aligned along x-axis and no-flux along the domain edges parallel to the deposition axis (z). The 2D simulation domain spans 200 × 200 grid-points along the x and z directions. For simplicity, we assume that the deposition temperature is sufficiently low to minimize lateral grain boundary motion. We simulate phase separation during vapor co-deposition by varying process parameters such as the deposition rate, v, bulk, and grain boundary atomic mobilities. Non-dimensionalized values of deposition and system parameters are listed in Table 1.

2.4. Incorporating film surface

In this section, we discuss a ternary Cahn–Hilliard model to explore the influence of surface contact angles on the nanostructural evolution of binary phase-separating alloys films (A-B) comprising of A-rich and B-rich domains, while the vapor constitutes the third phase [39,43,44]. The evolution of the film nanostructure is driven by a phenomenological minimization of the total free energy re-written as

$$F = \int_V N_v \left[f(\phi_A, \phi_B, \phi_v) + \kappa_A (\nabla \phi_A)^2 + \kappa_B (\nabla \phi_B)^2 + \kappa_v (\nabla \phi_v)^2\right] dV, \tag{20}$$

where, N_v is the number of molecules per unit volume (assumed independent of composition and position) and κ_i ($i = A, B$, and v) are the gradient energy coefficients associated with the concentration field. The order parameters, ϕ_A and ϕ_B, denote the scaled concentrations of the alloying elements, A and B in the film, while ϕ_v corresponds to the vapor phase which is in contact with the film's surface. In the interest of mass conservation, the sum of the order parameters is constrained to be unity by imposing

$$\phi_A + \phi_B + \phi_v = 1. \tag{21}$$

The chemical free energy per molecule, $f(\phi_A, \phi_B, \phi_v)$, corresponds to a regular solution, such that

$$\frac{1}{k_B T} f(\phi_A, \phi_B, \phi_v) = \sum_{i \neq j} \chi_{ij} \phi_i \phi_j + \sum_i \phi_i \log \phi_i, \tag{22}$$

where, χ_{ij} (i,j = A, B, v; $i \neq j$) is the pairwise interaction energy between the components, k_B is the Boltzmann constant, and T, the absolute temperature. An expanded form of Eq. (22) can be written as

$$f(\phi_A, \phi_B, \phi_v) = k_B T[\chi_{AB}\phi_A\phi_B + \chi_{Bv}\phi_B\phi_v + \chi_{Av}\phi_A\phi_v + \phi_A \log \phi_A + \phi_B \log \phi_B + \phi_v \log \phi_v]. \tag{23}$$

We can eliminate one of the field variables by replacing ϕ_v with $1 - \phi_A - \phi_B$ in Eq. (23), and rewriting it as

$$f(\phi_A, \phi_B) = k_B T[\chi_{AB}\phi_A\phi_B + \chi_{Bv}\phi_B(1-\phi_A-\phi_B) + \chi_{Av}\phi_A(1-\phi_A-\phi_B) + \phi_A \log \phi_A + \phi_B \log \phi_B + (1-\phi_A-\phi_B)\log(1-\phi_A-\phi_B)]. \tag{24}$$

The chemical potential of A-rich and B-rich phases are obtained by deriving the variational derivatives of the free energy functional in Eq. (22) with respect to ϕ_A and ϕ_B, such that

$$\mu_A = \frac{\delta F}{\delta \phi_A} = \frac{\partial f}{\partial \phi_A} - 2\kappa_{AA}\nabla^2\phi_A - 2\kappa_{AB}\nabla^2\phi_B \tag{25}$$

and

$$\mu_B = \frac{\delta F}{\delta \phi_B} = \frac{\partial f}{\partial \phi_B} - 2\kappa_{BB}\nabla^2\phi_B - 2\kappa_{BA}\nabla^2\phi_A, \tag{26}$$

where, $\kappa_{AA} = \kappa_A + \kappa_v, \kappa_{BB} = \kappa_B + \kappa_v$, and $\kappa_{AB} = \kappa_{BA} = \kappa_v$.

The kinetics of phase separation is given by

$$\frac{\partial \phi_i}{\partial t} = -\nabla \cdot J_i^{'}, \qquad i = A, B, v \tag{27}$$

where $J_i^{'}$ is the total flux of each component in the system. We adopt a formulation that incorporates the net vacancy flux, $J_\circ$, during the diffusion process as reported earlier by Kramer et al. [45,46] and Bhattacharyya et al. [47,48], to obtain the net flux of each component, i, given by

$$J_i^{'} = J_i + \phi_i J_\circ \qquad i = A, B, v. \tag{28}$$

J_i is given by

$$J_i = -M_i \nabla \mu_i \qquad i = A, B, v \tag{29}$$

where, μ_i and M_i are the chemical potential per site and Onsager coefficient of the i^{th} component, respectively. The vacancy flux, $J_\circ$, is given by

$$J_\circ = -(J_A + J_B + J_v). \tag{30}$$

By substituting Eq. (30) and (28) in Eq. (27) and using the Gibbs–Duhem relationship [46,48], we arrive at the following expressions for the temporal evolution of A- and B-rich phases:

$$\frac{\partial \phi_A}{\partial t} = M_{AA}\nabla^2\left[\left(\partial f/\partial \phi_A\right) - 2\kappa_{AA}\nabla^2\phi_A - 2\kappa_{AB}\nabla^2\phi_B\right] + M_{AB}\nabla^2\left[\left(\partial f/\partial \phi_B\right) - 2\kappa_{BA}\nabla^2\phi_A - 2\kappa_{BB}\nabla^2\phi_B\right] \tag{31}$$

and

$$\frac{\partial \phi_B}{\partial t} = M_{BB}\nabla^2[(\partial f \Big/ \partial \phi_B) - 2\kappa_{BB}\nabla^2\phi_B - 2\kappa_{BA}\nabla^2\phi_B] + M_{AB}\nabla^2[(\partial f \Big/ \partial \phi_A) - 2\kappa_{AB}\nabla^2\phi_B - 2\kappa_{AA}\nabla^2\phi_A], \tag{32}$$

where, M_{AA} and M_{BB} are the atomic mobilities of A and B atoms in non-A-rich and non-B-rich phases, respectively, while M_{AB} and M_{BA} are mobilities of A atoms in B-rich phase and B atoms in A-rich phase, respectively [46,47]. These are coupled to the diffusion coefficients of the alloying components, D_i, by extending the Nernst-Einstein relation to a ternary system [49],

$$M_{ii} = \frac{1}{k_B T} D_i \phi_i (1 - \phi_i) \qquad i, j = A, B, v \tag{33}$$

and

$$M_{ij} = \frac{1}{k_B T} D_i \phi_i \phi_j \qquad i, j = A, B, v \qquad i \neq j \tag{34}$$

We solve Eq. (31) and (32) by first non-dimensionalizing the parameters using the relation $l^* = (\kappa_i / 2k_B T)^{1/2}\Delta x$ and $t^* = (k_B T / M_{ii}^* l^{*2})$ where l^* and t^* are the characteristic length and time, respectively, and M_{ii}^* is the dimensional value of mobility for phases $i = A, B$. The dimensionless forms of the equations are solved via an explicit finite difference scheme for temporal and spatial derivatives.

In vapor-deposited films where the nanostructural evolution is characterized by the formation of phase-separating domains, interfacial energies play a dominant role in the morphological self-assembly. The role of excess energies at the interphase and surface boundaries can be quantified by measuring contact angle, θ, at the steady-state, which is governed by a balance of forces at the triple junction of A, B, and vapor phases. This is encapsulated within Young's equation as

$$\theta = 2\cos^{-1}\left(\frac{\sigma_{AB}}{2\sigma_{pv}}\right) \tag{35}$$

where θ is the surface contact angle, σ_{AB} is the interfacial energy between the phase-separated pure domains of A and B, while σ_{pv} equals the energy of film surface which is in contact with the vapor phase. Here, p denotes either the A-rich or the B-rich phase, depending on which of the two constitutes the surface that is in contact with the vapor. We would like to clarify that the interfacial energies of either domain that are in contact with the vapor are assumed to be equal, which in turn leads to the formation of symmetrical surface grooves.

Table 3
Interaction parameters and the measured dihedral angles from steady-state simulations shown in Fig. A.1.

Simulation	Interaction parameters	Measured θ
a	$\chi_{Av} = \chi_{Bv} = 2.7, \chi_{AB} = 3.5$	31.67°
b	$\chi_{Av} = \chi_{Bv} = 2.8, \chi_{AB} = 3.5$	50.90°
c	$\chi_{AB} = \chi_{Av} = \chi_{Bv} = 3.5$	117.16°

The excess energy at the interface between two phases, defined by components, A and B, is given by the expression [39],

$$\sigma_{AB} = 2N_v\lambda[k_B T]^{1/2}\int_{\phi_A}^{\phi_B}(f(\phi))^{1/2}d\phi \tag{36}$$

where N_v denotes the number of molecules per unit volume, and λ is the interaction distance, which is related to the intermolecular distance and is assumed to be a constant for the alloy. ϕ is the composition field that varies in magnitude from ϕ_A within the A-rich phase to ϕ_B within the B-rich phase. This equation is solved by approximating the interfacial energy based on the bulk free energy at its maximum value [39], given by

$$\sigma_{AB} \sim 2N_v\lambda[k_B T_C]^{1/2}\frac{\pi}{2}(\phi - \phi_e)[f(\phi)]_{max}^{1/2} \times \left[1 - \left(\frac{\pi}{2} - \frac{4}{3}\right)\frac{T}{T_c}\right] \tag{37}$$

where ϕ_e is the equilibrium value attained by ϕ when the system reaches a steady-state. In a binary system, a single order parameter, ϕ, which varies from A-rich and B-rich phases, is sufficient to define its compositional layout. However, in a three-component system with an additional vapor phase, the excess energy at the interface would depend on not one but two order parameters that operate independently from one another. This renders the calculation of interfacial energy from Eq. (36), and therein, the contact angle, non-trivial. However, a relationship between the excess energy associated with the interphase or surface boundaries and the interaction parameters corresponding to the alloy is known as per Eq. (37). We, therefore, assign a dihedral angle by tuning the values of the interaction parameters corresponding to the α-β and film-vapor interfaces. We assign $\chi_{AB} = 3.5$, while χ_{Av} and χ_{Bv} are assumed to be 2.7, 2.8, and 3.5. To accurately determine the dihedral angles that emerge by tuning the χ-values, we track the triple-point angle as the interfaces relax to a steady-state configuration. An in-depth discussion on determination of dihedral angles is provided in Appendix A. Based on the combinations of χ listed above, we deduce dihedral angles of 32°,51°, and 117°. Parameters assumed for simulating deposition using the phase-field model described in this section are listed in Table 3.

Phase-field simulations of PVD are performed in a three-dimensional domain with 150 grid-points each along the x- and the y-axes, and a maximum of 200 grid-point along the deposition axis, which is aligned along the z-direction. Grid-size in realistic lengthscale equals 1.1 nm, which is calculated based on observed interface widths and morphological phase-separated domains in vapor-deposited immiscible Cu-Mo and Cu-Ta alloys [27,21,50]. An initial condition, consisting of a seed layer of thickness $20\Delta z$ is used. The top half of the simulation space is assigned as the vapor phase, thereby allowing for a 50/50 split in the space by volume. To simulate deposition, a non-decomposed seed layer is added every few timesteps, $n\Delta t$, which leads to a temporal increase in the film's thickness. The seed layer is added at the juncture of the interface between the vapor and the film, at $\phi_v = 0.5$. To compensate for

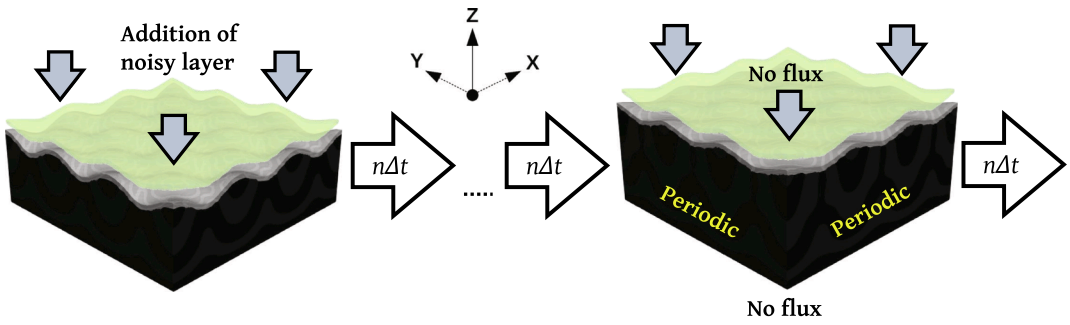

Fig. 2. Schematic diagram showing the surface undulation caused due to consideration of film surface in simulating the nanostructural evolution during PVD of binary alloy films. Deposition rate, $\upsilon = 1/n\Delta t$.

the loss in the relative volume of the vapor phase, the vapor half of the simulation box is incremented by $1\Delta z$. A schematic diagram illustrating this simulation technique is shown in Fig. 2. A complete specification of the thermodynamic and kinetic parameters incorporated in this model are listed in Table 1.

3. Results and discussion

In this section, we discuss the evolution of nanostructured domains in PVD of phase-separating alloy films as simulated using the models describe in the previous section. We first discuss the case of a simple monocrystalline film, where elastic misfit and surface effects are assumed to be negligible. Then we introduce the physics of elastic misfit, along with elastic anisotropy using the model outlined in Section 2.2, and discuss their effects on the evolution of characteristic nanostructures. We then extend our approach to account for film polycrystallinity and address the influence of grain boundaries on the evolution of nanostructured films. Finally, we explore the role of the film surface and the associate dihedral angles, in causing surface undulations and growth of protuberances that have previously been observed in experiments.

3.1. Influence of deposition rate and mobility

For the sake of context and completeness, here we briefly recapitulate our previous findings pertaining to vapor-deposited films of composition 50 at.% B [21]. At a mobility value, $M = 0.3$, and a slow deposition rate of $\upsilon = 0.089$, the film self-assembles into LCM, where the α and the β domain boundaries that are aligned parallel to the deposition axis are bi-continuous in the perpendicular 2D slices, as shown in Fig. 3(a). Isosurfaces representing the α-β interface of the LCM nanostructures appear to be vertically-oriented (Fig. 3(d)), revealing the bi-continuous characteristic along the horizontal plane. This bi-continuity remains largely intact with an increase in the film thickness. A slow deposition rate, in this case, ensures that the co-deposited elements phase-separate into α and β regions well before new layers have been added, which ultimately results in a lateral domain alignment where penultimate layers serve as a template to drive successive phase separation in the freshly deposited layer.

Increasing the deposition rate to $\upsilon = 0.2$, without altering the composition or mobility, yields VCM nanostructures where the concentration modulations are observed across α and β layers stacked along the deposition axis, as depicted in Fig. 3(c). The alignment of interfaces in the vertically-modulated structure in Fig. 3(f) shows a periodic oscillation of concentrations along the deposition axis. A faster deposition rate does not allow the preexisting layers to achieve their respective equilibrium concentration values. This leads to an interlayer diffusion between the penultimate and the freshly deposited layers, ultimately causing VCMs.

At $\upsilon = 0.133$, a mixed structure that comprises of a mixture of the VCMs and LCMs, evolves, as shown in Fig. 3(b). The alternating blue and red isosurfaces in Fig. 3(e) show an initial tendency toward the formation of VCM regions, which then transition into green isosurfaces representing an LCM interface towards the top. Such a mixed morphology is found to evolve in a narrow region sandwiched between VCM and LCM in the morphology map shown in Fig. 3(i).

Decreasing the mobility to $M = 0.2$ and increasing the deposition rate to above $\upsilon = 0.25$ results in decomposition from an ordered VCM morphology to a random bi-continuous nanostructure without any evident self-assembly, as seen in Fig. 3(g). This is substantiated by 3D-modulated interfaces in Fig. 3(h) that grow finer in the upper layers of the film. Evidence of such a morphology can be seen in the RCM morphologies of Cu-Mo films [21], where the films more closely resemble the nanostructures that may arise in bulk processing, such as in spinodal alloys.

An in-depth parametric study performed within a range of deposition rates and mobilities yields a morphology map that demarcates film morphologies as a function of these parameters, as shown in Fig. 3(i). This map depicts the range of processing parameters for which the LCM, VCM, mixed LCM-VCM (L-V), and the random (R) nanostructures evolve. When $\upsilon = 0.15$, random nanostructures evolve at low $M = 0.1$, LCMs at high $M = 0.5$, and mixed (L-V) and VCMs in the intermediate mobility ranges. The mixed nanostructures are observed in a narrow region bounded by the formation of LCMs and the VCMs. However, this region appears to broaden as the mobility increases. Overall, we observe that the morphology map shifts upward as the mobility increases. Our simulation-based insights are duly corroborated by experimental findings reported in [21], where the formation of all these distinct morphologies appear to be strongly dependent on temperature, which is related to atomic mobility, at an equal deposition rate.

3.2. Influence of elastic mismatch and elastic anisotropy

We first discuss the three cases of elastic anisotropy, the parameters for which are listed in Table 2. Following this, we evaluate the effect of elastic anisotropy on the interface orientation in LCM and VCM nanostructures. We then study the effect of deposition rate on phase separation and deduce a parametric space where anisotropic effects on the domain formation are negated by deposition rate. We maintain a constant ϵ^0_{ik} of -0.15% for all simulated deposition studies in this section.

When the film is elastically homogeneous, the morphology of the evolving film shows almost no deviation when compared to corresponding nanostructure simulated using the preliminary model reported in Section 3.1. As shown in Fig. 4(a), LCM and VCM nanostructures form at small and large deposition rates, respectively. However, the deposition rates required to obtain either of these nanostructures is notably larger, when compared to the ones in Fig. 3i. In fact based on a side-by-side comparison of film nanostructures, we observe that a large eigenstrain, which is associated with the elastic misfit, slows down the kinetics of phase separation, leading to a net increase in deposition rates at which LCM and VCM nanostructures evolve.

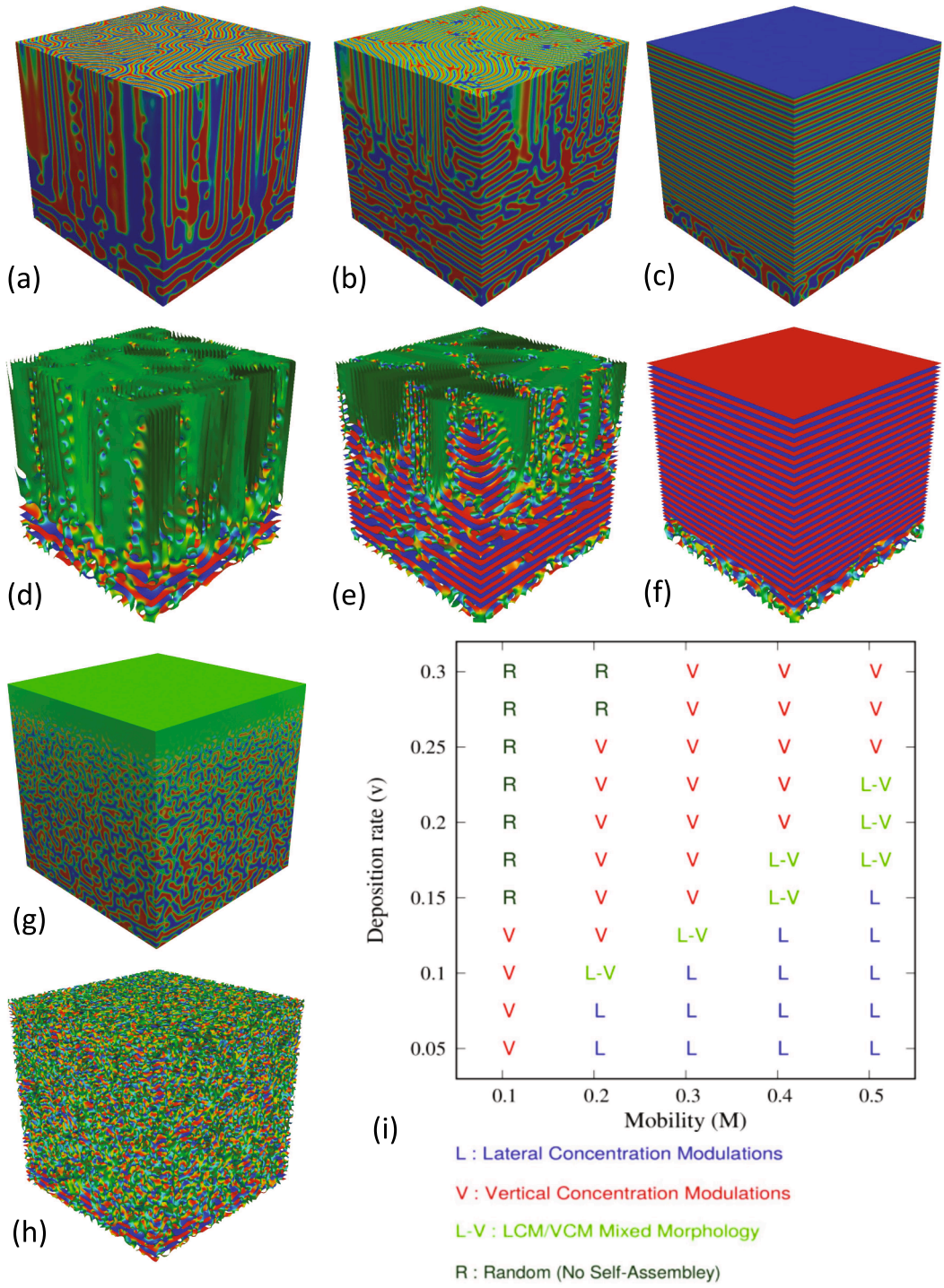

Fig. 3. Morphological evolution of films of 50 at.% B composition. Side view of 3D film nanostructures of 50 at.% B composition. The different morphologies that evolve are (a) LCM, (b) VCM, (c) mixed LCM and VCM, and (g) random bicontinuous. (d), (e), (f) and (h) show isosurfaces representing α-β phase boundaries. (i) shows a process-dependent morphology map generated based on a parametric study for a film of composition, 50 at.% B.

In the second case study shown in Fig. 4(b), the film is assumed to be elastically inhomogeneous and anisotropic such that the bulk moduli of the decomposing phases are highly disparate. We incorporate an anisotropy of $\xi_K^{\alpha}, \xi_K^{\beta} = 0.44, 2.80$, while maintaining the same ϵ_{ik}^{0}. We observe that cube-shaped domains of the α-phase evolve within a matrix of the softer β-phase at a low deposition rate, while layered domains are observed to a limited extent at a higher deposition rate (Fig. 4(b)). A complete absence of LCM nanostructure at low deposition rates infers a dominating influence of elastic anisotropy on morphological evolution as it penalizes the formation of interfaces along the deposition axis. A cubical shape of the harder α phase shows that elastic relaxation along the principal axes is responsible for this phenomenon. It must be noted that although the elastically favorable directions for the α-phase lie along the {11} crystallographic planes, the cubic domains tend to show a preference for alignment parallel to the {10} and {01} planes during film deposition, a trend which is also seen in bulk phase-separations in alloys with elastic anisotropy due to the bulk modulus [51]. However, at a faster deposition rate, VCM nanostructures continue to evolve,

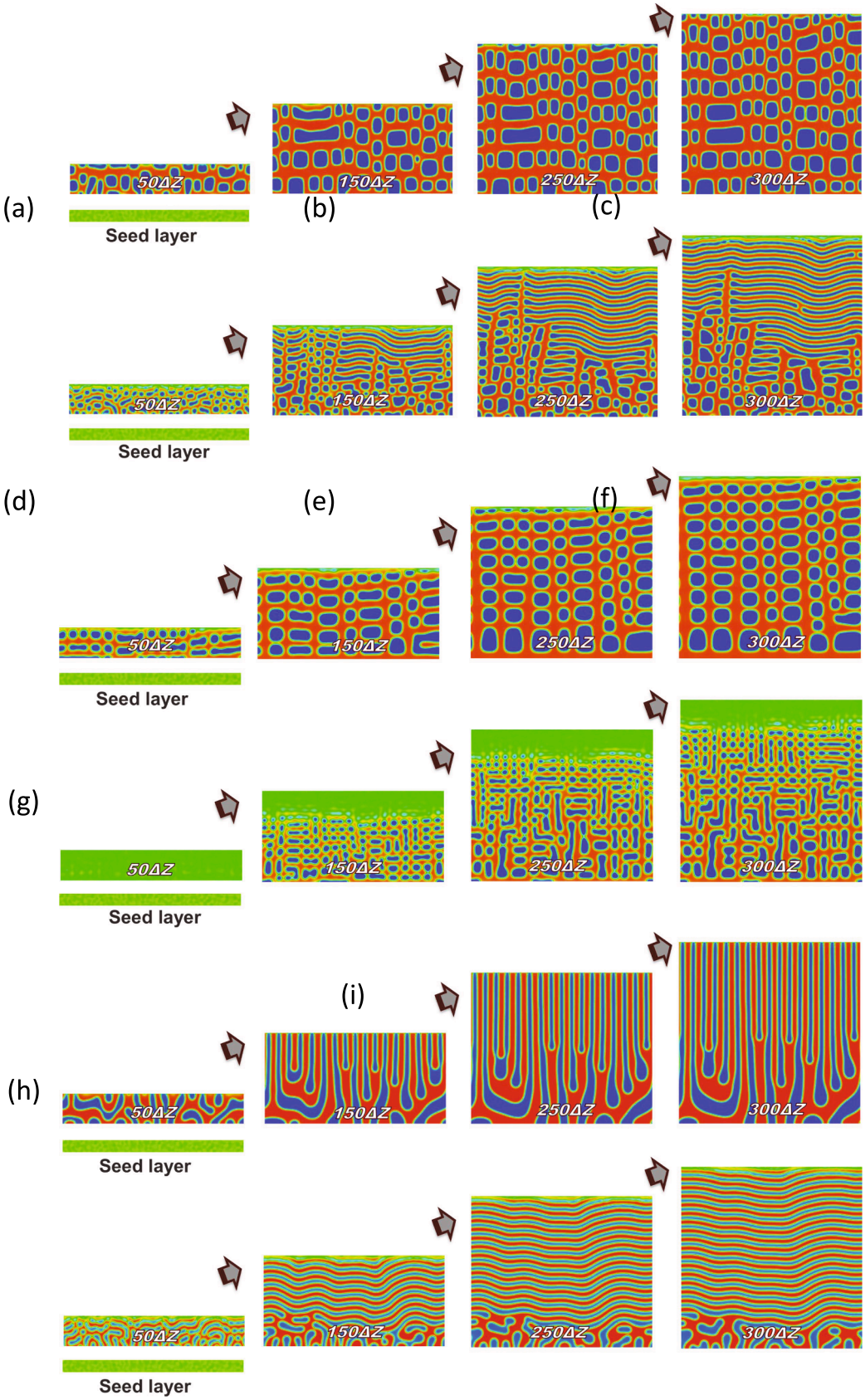

Fig. 4. Morphological evolution of films of 50 at.% B composition. (a) Elastically homogeneous and isotropic film deposited at $\upsilon = 0.04$ (above) and $\upsilon = 0.2$ (below), (b) Non–homogeneous film with elastic anisotropy due to bulk modulus (ξ_K^α, $\xi_K^\beta = 0.44, 2.80$) deposited at $\upsilon = 0.04$ (above) and $\upsilon = 0.2$ (below), and (c) Non–homogeneous film with elastic anisotropy due to shear modulus ($\xi_s = 2.66$) deposited at $\upsilon = 0.04$ (above) and $\upsilon = 0.2$ (below). $\epsilon_{ik}^0 = -0.15\%$. Initial condition for every simulation above is composed of a noisy seed layer of thickness $20\,\Delta z$. Arrows indicate axes and planes.

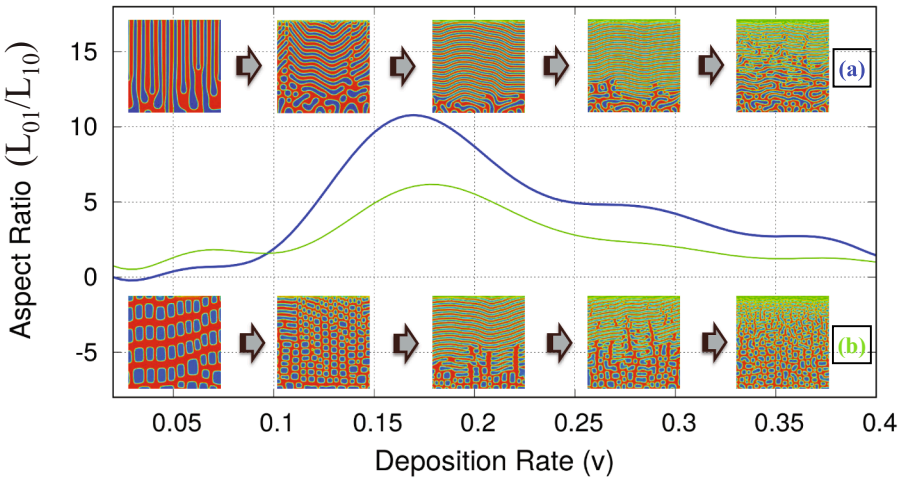

Fig. 5. Interface orientation measured as a function of deposition rate for (a) Homogeneous and elastically isotropic film, (b) Non–homogeneous film with elastic anisotropy due to bulk modulus ($\xi_K^{\alpha,\beta} = 0.44, 2.80$). $\epsilon_{ik}^0 = -0.15\%$.

suggesting that for this case, the time available for elastic relaxation before a new layer is deposited is smaller. Thus, at such fast deposition rates, the formation of nanostructure proceeds similar to elastically isotropic films.

When the film is assumed to be elastically inhomogeneous and anisotropic, the latter arising due to a large difference between the shear moduli of the two decomposing phases, the morphology of the evolving film is distinct when compared to preceding cases, as shown in Fig. 4(c). Here, we incorporate a shear anisotropy of $\xi_s = 2.66$ while the ϵ_{ik}^0 is unchanged. However, it is coupled to the shear moduli and therefore impacts the phase evolution along both axes. At slow deposition rates, the harder α-phase form cubic domains, with a preferential alignment parallel to the elastically favorable $\{10\}$ and $\{01\}$ crystallographic planes. At a faster deposition rate, we observe domains of the hard phase that appear similar to those observed during phase separation under a comparatively lower shear anisotropy. This result suggests that fast deposition rates may not allow the formation of layered morphology, similar to the second case, but does mitigate the influence of elastic anisotropy caused due to shear moduli.

To characterize the simulated nanostructures based on interface orientation, we employ a dimensionless aspect ratio metric [40,37], which is defined by the following expression,

$$AR = \frac{L_{[01]}}{L_{[10]}}, \tag{38}$$

where $L_{[01]}$ denotes the component of the $\alpha-\beta$ interface which is oriented primarily along the direction of the [01]-crystallographic plane, and $L_{[10]}$ denotes the component of the interface which is oriented primarily along the direction of the [10]-crystallographic plane. The orientation relationship between an unknown interface orientation and the gradient of the phase-field parameter, ϕ is given by the unit vector,

$$\hat{n} \equiv \frac{\vec{\nabla}\phi}{|\vec{\nabla}\phi|}. \tag{39}$$

The length of interfaces oriented along a crystallographic plane parallel to the unit vector, $\hat{o}$, is calculated using [40],

$$L_{\hat{o}} = \frac{1}{2w}\int \{h(\phi)h(1-\phi)\,\Theta(\hat{n}.\hat{o} - cos(\vartheta))\}dV, \tag{40}$$

where w is the interface width and $\Theta(x)$ is a step-function which assumes a value of 1 if $x \leqslant 0$ and 0 if $x > 0$. ϑ, which quantifies the uncertainty angle that is used to determine the interface orientation, is assigned a value of $\pi/4$ in all the simulations reported in this section. A plot of the effect of elastic anisotropy due to bulk moduli ($\xi_K^{\alpha,\beta} = 0.44, 2.80$) on the aspect ratio of phase-separating domains is shown in Fig. 5. When comparing the alignment of interfaces in Fig. 5(a) with 5(b), it can be inferred that the presence of elastic anisotropy significantly impacts the film's nanostructure as depicted by a lowering of the peak aspect ratio. This finding strongly supports our hypothesis that elastic anisotropy modulates the transition from classical LCM to VCM nanostructures of phase-separating alloy films. Upon plotting the temporal evolution of strain gradients during the annealing of a film deposited at $v = 0.04$, we observe the direction of diffusional flux pointing towards the softer phase, as shown in Fig. 6. As time evolves, the diffusion of atoms causes the re-assembly of the VCM layers into cubical domains. During evolution, misfit strains within the film are minimized, as seen by the net reduction in the strain energy gradient in the illustrated region of the film. This behavior confirms our hypothesis that a faster deposition rate does not allow sufficient time for strain-relaxation to fully occur, due to which VCM-like nanostructures form, as shown in Fig. 6(a). However, when the film is annealed, the strain-relaxation that guides the atomic diffusional flux facilitates a transition from VCM to a cubic nanostructure.

3.3. Influence of grain boundaries

In this section, we discuss the implications of incorporating grain boundaries into our model, as described in Section 2.3, and how they impact the formation of phase-separating domains. We first simulate the evolution of these nanostructured domains in polycrystalline films deposited at distinct rates. It is well known that grain boundaries provide fast atomic diffusion pathways. Therefore, our model assumes that the atomic mobility of atoms within the grain is three orders of magnitude smaller than the corresponding value along the grain boundaries, or $M_b = 0.005 M_{gb}$. To avoid any complexities caused due to grain coarsening, the grain boundaries are rendered immobile by assuming a small relaxation coefficient, $L = 0.1$. Under these assumptions, we observe LCM nanostructures forming along the grain boundaries, regardless of the deposition rate, as shown in Fig. 7. At a moderate deposition rate of $v = 0.005$, the width of the LCM region is narrowed with the VCMs forming predominantly away from the grain boundaries. Such a film morphology, where the VCMs are confined within LCMs, is reminiscent of the mixed nanostructure simulated in absence of grain boundaries, as shown in Fig. 3(b) and (e). At a fast deposition rate of $v = 0.014$, VCMs in the grain interior gives way to a random bicontinuous nanostructure that is confined within the LCMs forming adjacent to the

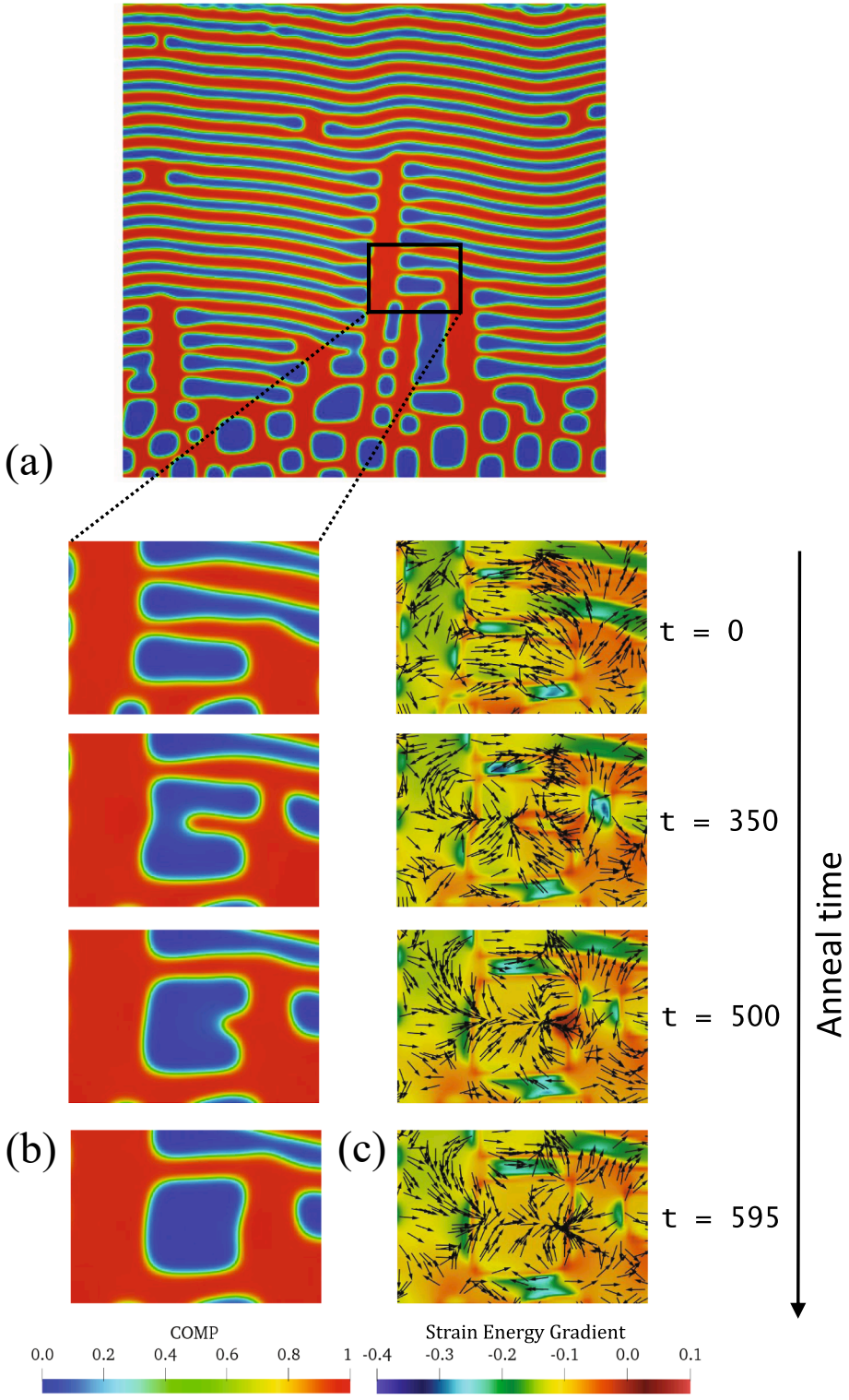

Fig. 6. Effects of annealing on domain restructuring in film with elastic anisotropy due to bulk modulus (Fig. 4b) deposited at $v = 0.04$. (a) shows the as-deposited film, (b) depicts a small region of (a) where VCM layers of the α (blue) phase reorganize into a cubic domain during annealing. (c) shows arrows indicating the direction of atomic flux guided by the s.train gradients.

grain boundaries. From these observations, we infer that assuming a large M_{gb}/M_b ratio, which renders the mobility of atoms within the film, non–homogenous, causes the formation of such mixed nanostructures. Clearly a larger M_{gb} relative to the M_b ensures that phase separation starts along the grain boundaries, as the decomposition in the grain interior lags, resulting in the confinement of VCM and random nanostructures.

To better understand the competing mechanisms of phase separation at the grain boundaries and grain interior, we assume that the atomic mobility of atoms within the grain is now two orders of magnitude smaller than the corresponding value along the grain boundaries, or $M_b = 0.06M_{gb}$, while all other simulation parameters remain un-

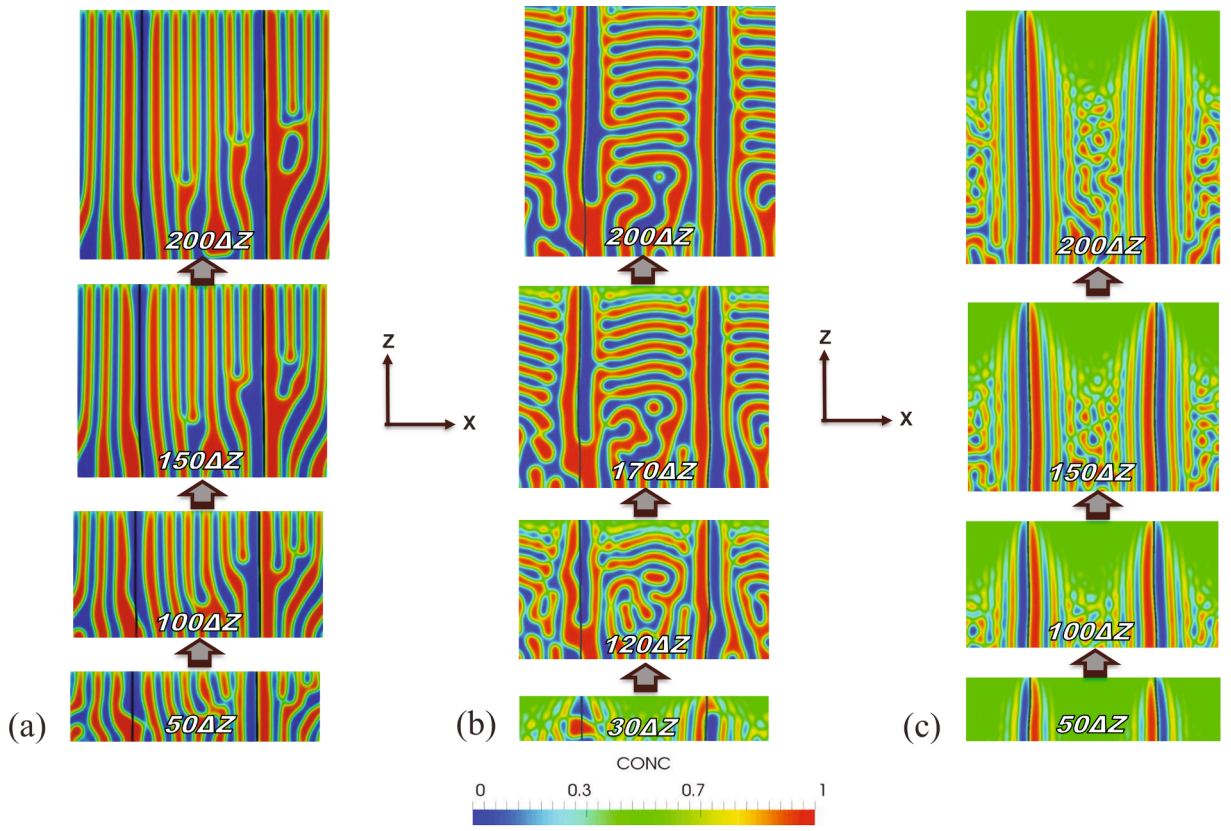

Fig. 7. Morphological evolution of polycrystalline films of 50 at.% B composition, grain-width 50 nm for atomic mobility ratio, $M_b/M_{gb} = 0.005$, and $L = 0.1$ at (a) slow deposition rate, $v = 0.0025$, (b) medium deposition rate, $v = 0.005$, and (c) fast deposition rate, $v = 0.014$.

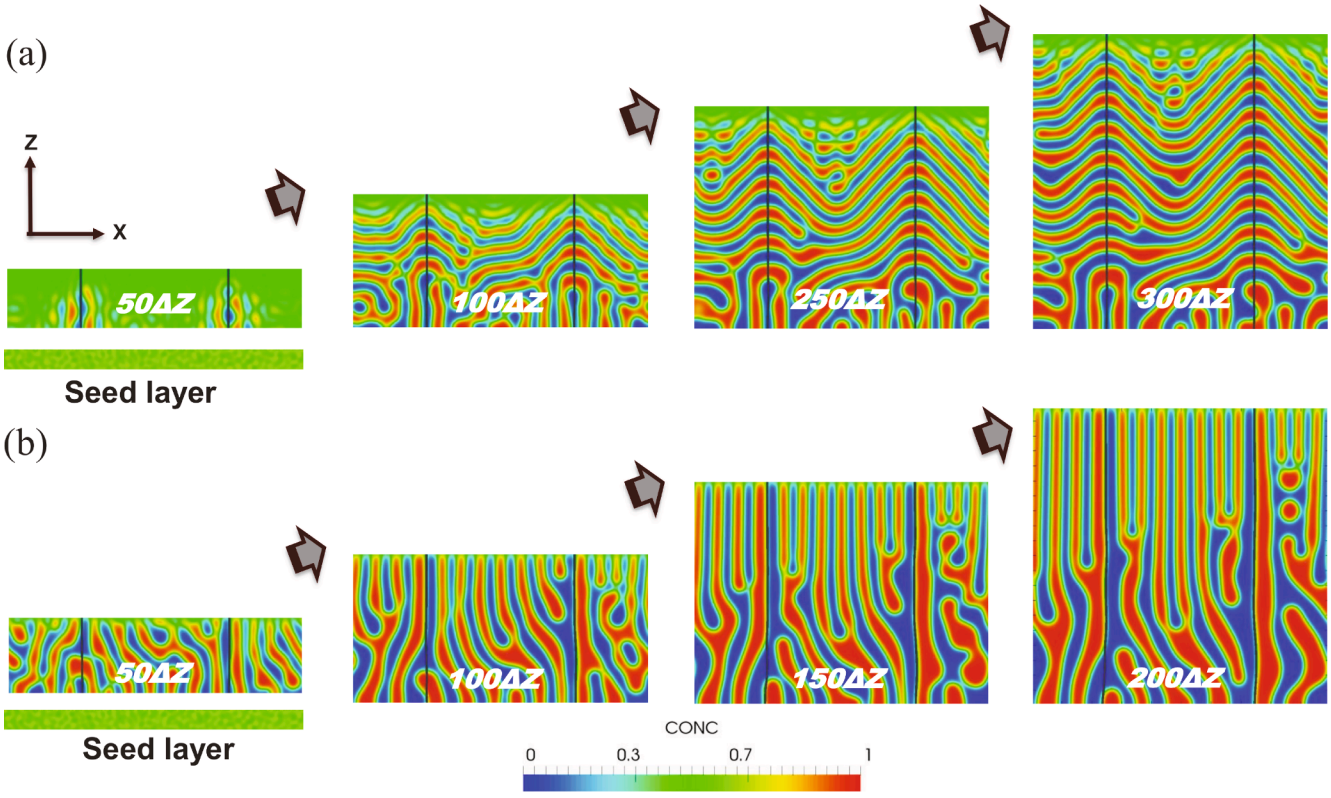

Fig. 8. Morphological evolution of polycrystalline films of 50 at.% B composition and grain-width 50 nm corresponding to atomic mobility ratio, $M_b/M_{gb} = 0.06$, and $L = 0.1$ at (a) fast deposition rate, $v = 0.2$, and (b) slow deposition rate, $v = 0.09$.

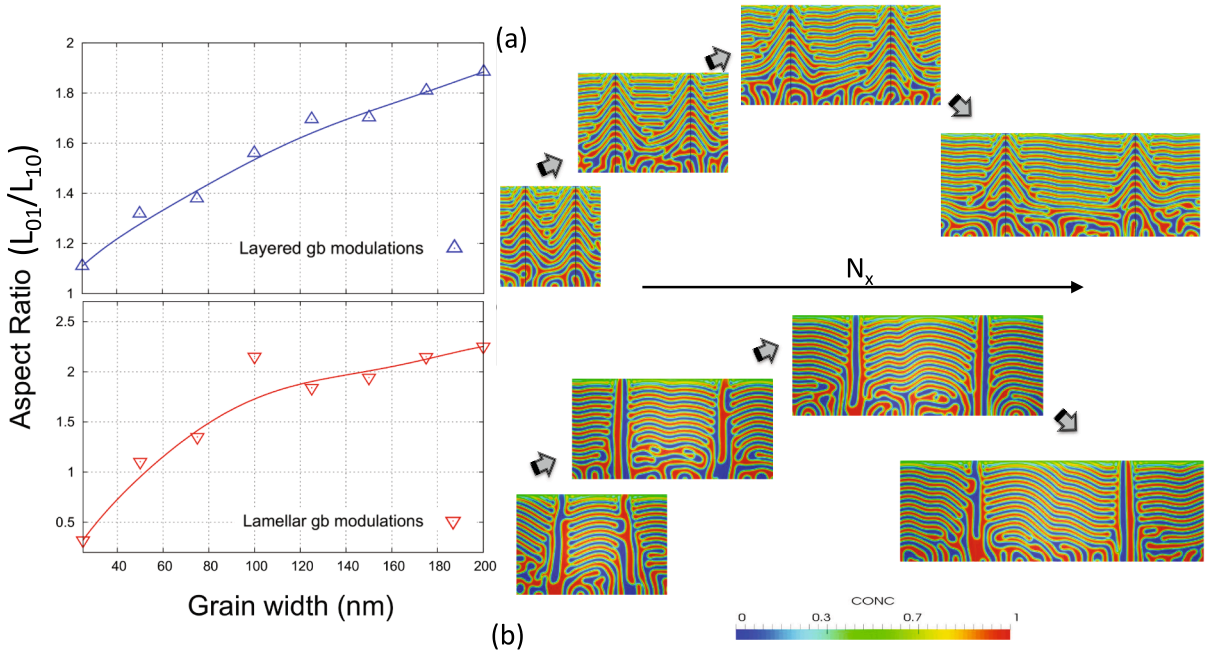

Fig. 9. Interface orientation in polycrystalline films measured as a function of the grain size for (a) $M_b/M_{gb} = 0.06$ and $L = 0.1$ at $\upsilon = 0.2$, and (b) $M_b/M_{gb} = 0.002$ and $L = 0.1$ at $\upsilon = 0.005$.

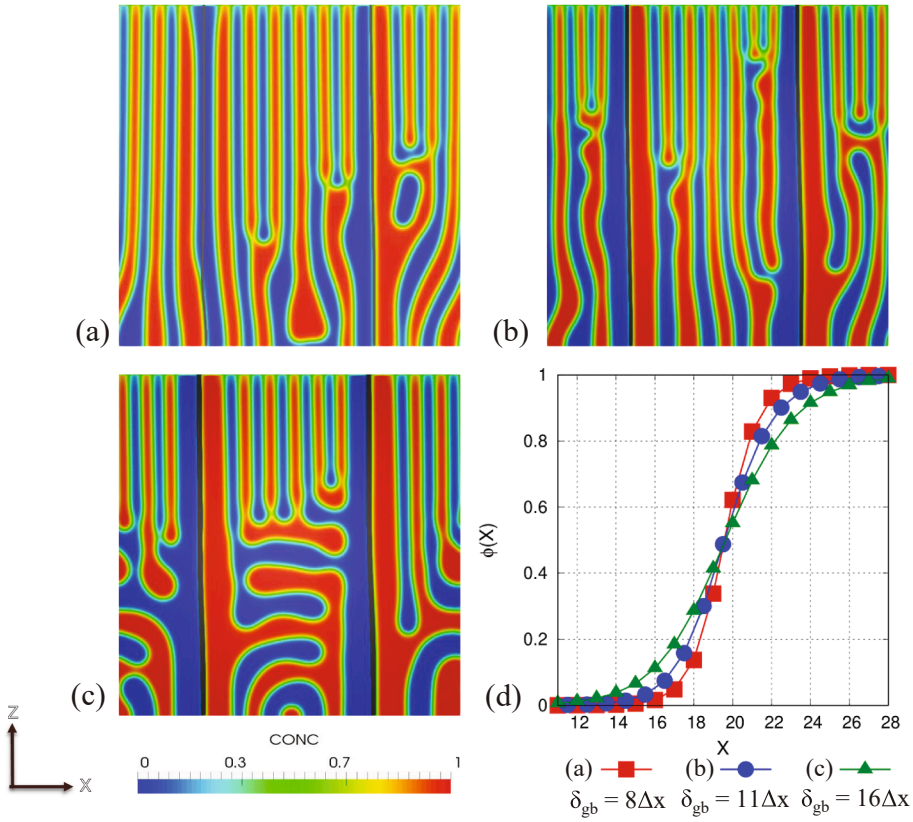

Fig. 10. Morphology of film nanostructures simulated by assuming distinct grain boundary widths, δ_{gb}, that equal (a) $8\Delta x$, (b) $11\Delta x$, and (c) $16\Delta x$. (d) Corresponding variations of η plotted orthogonal to the grain boundary. Other simulation parameters correspond to Fig. 7(a), where $M_b/M_{gb} = 0.005, L = 0.1$ and $\upsilon = 0.0025$.

changed. Under these conditions, we note that phase separation first occurs along the grain boundaries. However, at a fast deposition rate, $\upsilon = 0.2$, VCM-like nanostructures start to evolve at grain boundaries, as opposed to LCM. This leads to the formation of undulated VCM nanostructure which resembles chevron patterns, that have previously been reported to exist in PVD nanostructures of Cu-Fe films by Derby et al.

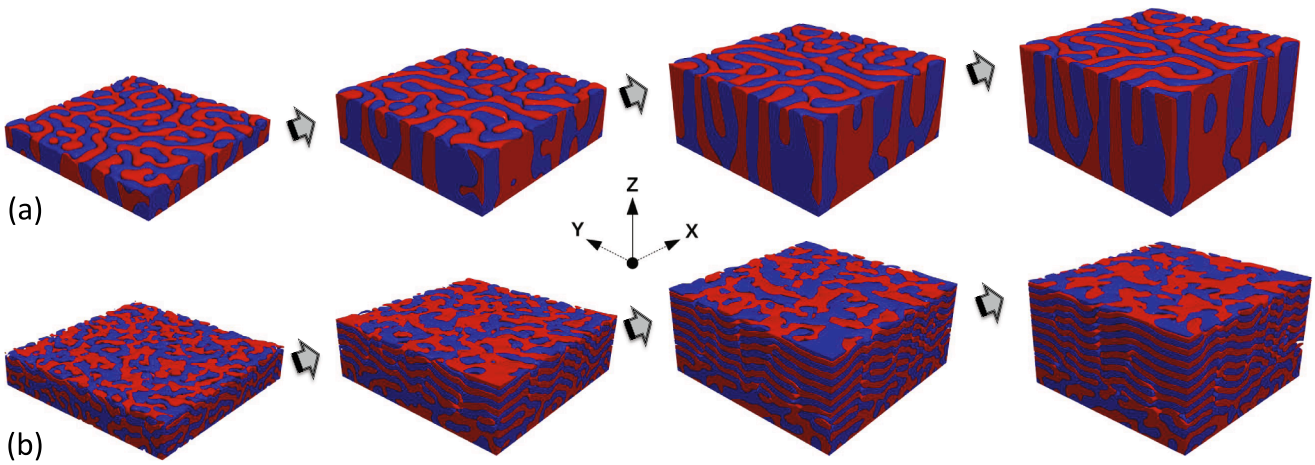

Fig. 11. Evolution of phase-separated domains in codeposited films with a free surface exposed to the vapor phase with a contact angle, $\theta = 120^{\circ}$. Deposition rates (a) $\upsilon = 0.05$, and (b) $\upsilon = 0.5$. A-rich phase is shown in blue while the B-rich phase in red.

[52]. The characteristic V-shape of these nanostructures can be observed in our phase-field simulations reported in Fig. 8(a). However, chevron VCMs give way to LCMs when υ is reduced by half, as shown in Fig. 8(b). Apparently, deposition rate plays a crucial role in the simulated transition from a chevron VCM to LCM film nanostructure. Additionally, the amplitude of undulations in chevron VCMs are observed to be sensitive to grain size which implies grain boundary confinement of film nanostructures. Increasing the M_b by an order of magnitude causes this confinement effect of grain boundaries to cease, such that the nanostructural transitions are no longer affected by grain size. To evaluate the effect of grain size on the orientation of interfaces in these nanostructured films, we apply the same aspect ratio metric that was used in Section 3.2 to characterize interfaces orientation. Based on this metric, a larger aspect ratio is expected when the interfaces are primarily oriented perpendicular to the deposition axis (vertical). On the contrary, a predominant alignment of interfaces along the deposition axis would lead to smaller aspect ratios. As shown in Fig. 9(a), we observe that the spacing between chevron or V-shaped undulation increase with grain size resulting in a steady increase in the aspect ratio. A similar trend is also observed for VCM film nanostructures, as shown in Fig. 9(b).

Finally, to ascertain the role of grain boundary width, δ_{gb}, on the evolving nanostructures, we perform phase-field simulations of LCM growth by assuming distinct grain boundary width, δ_{gb}. Although the morphologies of deposited films simulated at distinct δ_{gb} are distinguishable from one another, the LCM nanostructure is found to remain intact. However, in such cases, the thickness of the deposited film becomes of paramount importance since assuming a larger interface width that is related to grain boundary interfacial energy, alters the ratio of surface and interfacial energies, which ultimately determines the film thickness at which VCM to LCM transitions occur, as simulated in Fig. 10 (c).

3.4. Influence of vapor phase

Based on the no-flux boundary conditions imposed along the top edge of the computational domain, all the above-reported phase-field

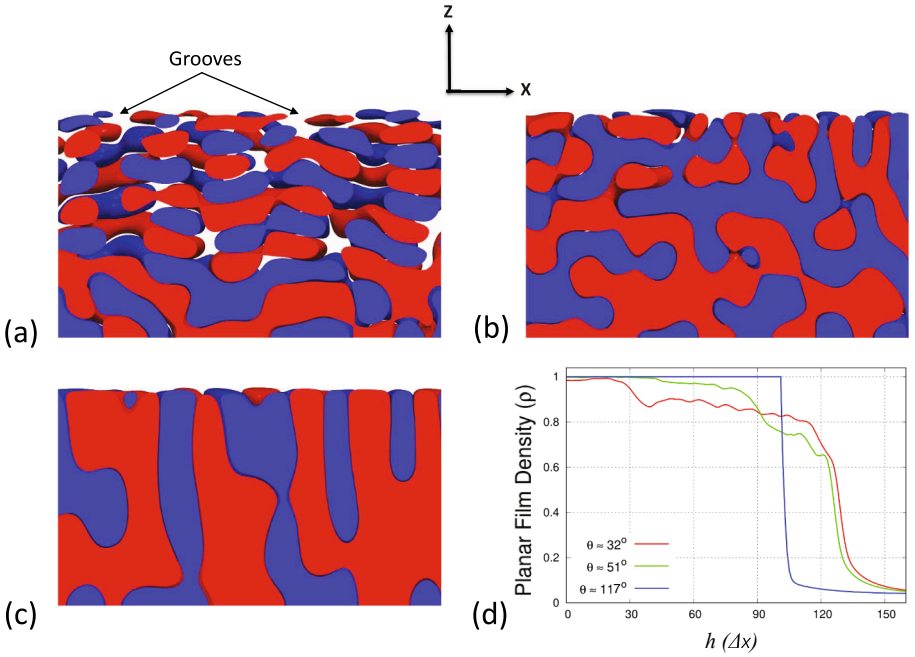

Fig. 12. 3D simulations showing the phase-separated nanostructured domains in simulated films at different dihedral angles (a) $\theta \sim 32^{\circ}$, (b) $\theta \sim 51^{\circ}$, and (c) $\theta \sim 117^{\circ}$. (d) shows a plot of the film density as a function of film height, h (given in terms of grid spacing, Δx).

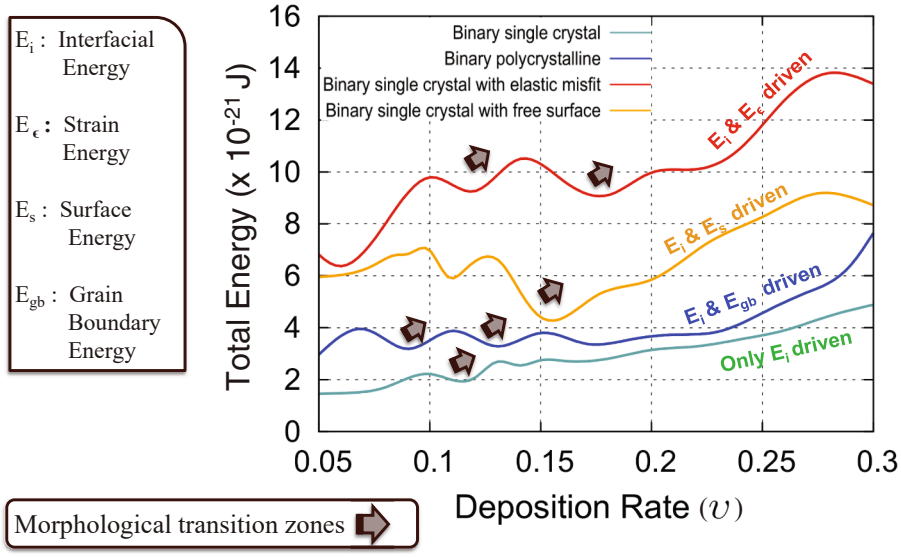

Fig. 13. Total film energies (E) plotted as a function of deposition rate (υ) corresponding to nanostructures simulated using the models described in Sections 2.1, 2.2, 2.3, and 2.4. Arrows indicate the deposition rate at which morphological transitions occur.

simulations implicitly assume a dihedral angle of 180°. Thus, we ignore the role of the film surface, particularly the dihedral angle, that can influence phase separation of nanostructured domains during PVD. Here, we examine the influence of surface energy by simulating the nanostructural evolution of vapor-deposited films at distinct deposition rates. First, we impose a dihedral angle equal to 117° by assuming $\chi_{AB} = \chi_{Av} = \chi_{Bv}$, and simulate phase separation during co-deposition in a three-phase system with two alloy phases and a vapor phase, as described in Section 2.4. At a slow deposition rate, $\upsilon = 0.05$, the phase-separating domains evolve into a LCM morphology (Fig. 11(a)). However, at $\upsilon = 0.5$, a VCM nanostructure evolves (Fig. 11(b)). The surface grooves that form at the triple-junction of phase-separated domains and the vapor phase are predominantly observed in LCM film nanostructures.

While the deposition rate and atomic mobility govern nanostructural evolution in PVD films, the ratio of surface and the domain boundary energies impacts the dihedral angle, thereby giving rise to surface undulations and grooves. However, it is remarkable that by merely altering this ratio such that $\theta \sim 0°$, distinct film nanostructure replete with crevices, protuberances, and voids form, as shown in Fig. 12(a). When $\theta \sim 51°$, the surface undulations and voids within the thickness of the film, decrease. At a larger $\theta \sim 117°$, the film is almost entirely free of voids and undulations. Our observations are confirmed by the plot of the planar film density, ρ, as a function of the film height, as shown in Fig. 12(d). Here, ρ measures the normalized density of the film in a 2-D plane perpendicular to the deposition axis, and ranges from a maximum value of 1.0 in planes with no voids, to a lower limit below 0.1, which represents the vapor phase. When $\theta \approx 32°, \rho$ decreases steeply from a maximum value of 1.0 at $h = 30\Delta x$. At $\theta \approx 51°, \rho$ drops more gently with an increase in film thickness. When $\theta = 117°$, ρ maintains a constant value of ~ 1.0 within the thickness of the film and drops to its lowest value closer to the surface.

3.5. Criteria for morphological transitions

In analyzing the different nanostructural variants that evolve in our phase-field simulations, we note that the phase separation of domains is primarily guided by deposition rate and atomic mobility. Additionally, elastic properties, the presence of grain boundaries, and the grooving of film surface are also found to impact the evolution of film nanostructures. The distinct modeling approaches reported in this work allow us to explore the influence of each of these phenomena in isolation, thereby, advancing our basic understanding of mechanisms of phase separation in vapor-deposited alloy films. However, at the same time, it also presents us with the challenge of deducing a common underlying criterion that governs nanostructural self-assembly during PVD. Therefore, to address this challenge, we finally plot the total energy of the films, which may comprise of chemical, interfacial, and elastic energies depending on the model, as a function of the deposition rate, as shown in Fig. 13. In doing so, we ensure that the simulation data, although obtained using distinct models, incorporate a common set of process and material parameters, including the atomic mobilities, interfacial energies, and the simulation domain size. We observe that as the deposition rate increases, the total energy first increases followed by intermittent dips, before starting to increase again. Although the magnitude of energies varies across models, we observe that morphological transitions irrespective of the model always occur at extrema. For the preliminary model described in Section 2.1, the LCM transitions into VCM at $\upsilon = 0.14$, which corresponds to the value of deposition rate where the slope changes. For the polycrystalline model described in Section 2.3, we observe multiple peaks and troughs within this region, indicating that the presence of grain boundaries can cause several nanostructural transitions during PVD. The plot of total energy corresponding to the elastic misfit model described in Section 2.2 shows a trend similar to the preliminary model around $\upsilon = 0.1$ and 0.14, however, the variation of energies across different nanostructural variants of the deposited film are found to be larger. The overall energy of the film is also found to be the maximum of all the other models considered, given that the elastic energy is added to the interfacial and chemical energy densities, as indicated by the free energy functional 6. On the contrary, upon accounting for film surface using the model described in Section 2.4, the nature of the plot appears to be distinct with respect to other models since morphological transitions, in these cases, are now also guided by the variations in surface energy which is added within the total energy density, as per functional 20. A second commonality among the different models is the overall increase in the energy of the film as the deposition rate increases, as the number of extrema reduces. In all certainty, such a trend indicates a predominance of kinetics, particularly deposition rate, over thermodynamic factors, such as interfacial and chemical free energies, in determining the self-assembly of film nanostructures. Smaller numbers or a complete absence of peaks at large deposition rates imply an interesting nanostructural selection phenomenon when the processing is dominated by kinetic factors, as opposed to other variants that evolve at slow deposition rates. Raghavan et al. [24]

hypothesized in prior work, that with increasing deposition rates, morphological transitions in phase-separating films are driven by an intrinsic need to minimize the domain boundary energy. In this study, we observe evidence validating the hypothesis while asserting the role of elastic energy, grain boundary energy and surface energy, which along with the domain boundary energy, drive the morphological transitions that facilitate total energy minimization.

We note that morphological transitions in phase-separating films under experimental conditions may exhibit different degrees of the morphological transitions and domain-specific features discussed in the previous sections because the phenomenon is governed by numerous other deposition-related and material-specific parameters which are beyond the scope of this article. For instance, we have not considered the angle of approach of the elemental components when they impinge upon the film surface. We also do not take into account dislocations, and other kinds of defects that commonly plague monocrystalline and polycrystalline films. However, we believe that such processing complexities do not alter the underlying theory of morphological transitions that are typically observed at extrema corresponding to low deposition rates, as plotted in Fig. 13. Furthermore, complex hierarchical structures with multiple length-scales, such as the Cu-rich islands and Mo-rich FCC-superlattice structures within the Cu-rich islands, as observed by Derby et al. [53] have not been explored in this article. Modeling efforts in these directions are ongoing and shall be reported in future publications.

4. Conclusions

We have demonstrated several approaches for simulating nanostructural evolution in phase-separating binary alloy films during PVD. Our phase-field models which incorporate the multiphysics of elastic misfit and anisotropy, grain boundaries and free surface neatly capture the interplay of thermodynamical and kinetic factors that govern phase separation for a range of deposition rates. The preliminary model showed an evolution of distinct self-assembled morphologies such as LCM and VCM, along with mixed nanostructures and random bicontinuous nanostructures. Based on parametric studies, we characterize the distinct film morphologies and establish nanostructure-processing relationships using morphology maps.

The elastic misfit model increases the complexity of the *preliminary* model, by accounting for elastic heterogeneity and anisotropy in the film. We observe that cube-shaped domains of the hard phase form at slower deposition rates, while the VCMs are favored at faster deposition rates. However, upon annealing, VCM self-assemble into cubic domains that align along the principal strain axes. Our findings indicate that a faster deposition rate does not allow sufficient time for strain-relaxation to fully occur, while the strain-relaxation that occurs during the post-deposition annealing facilitates a transition from VCM to a cubic nanostructure.

Our phase-field model which accounts for grain boundaries by incorporating short-circuit diffusion pathways highlights the physics of confinement of nanosized domains that evolve during PVD of phase-separating alloys depending on the grain size and the ratio of atomic mobilities. For the first time, we explain the mechanisms by which chevron VCMs form and how grain size influences the evolution of such novel nanostructures. Our phase-field approach which explicitly models the vapor-film interaction shows the importance of small dihedral angles which leads to the formation of surface grooves, voids, and protuberances. However, immiscible alloy films comprise of a multitude of heterogeneous interfaces, the physics of which, in future, can be incorporated in the models reported here.

Finally, we post-process the simulation data gathered using distinct multiphysics modeling approaches to deduce unified criteria, which is based on total energy minimization, that governs nanostructural transitions during PVD of binary phase-separating alloy films. Our parametric studies infer that the evolution of nanostructured domains in films deposited at slow rates is primarily guided by the minimization of elastic energy in conjunction with the interfacial energies, that constitute the total free energy. However, at faster deposition rates and temperature, the nanostructure selection and formation proceeds via an interplay of these kinetic factors.

5. Data availability statement

The authors confirm that the data required to reproduce the findings of this study are available within the article and can be reproduced by phase-field simulations.

CRediT authorship contribution statement

Rahul Raghavan: Investigation, Software, Writing - original draft. **William Farmer:** Investigation, Software, Writing - original draft. **Leslie T. Mushongera:** Writing - review & editing, Supervision. **Kumar Ankit:** Conceptualization, Writing - review & editing, Funding acquisition, Supervision, Project administration.

Declaration of Competing Interest

The authors declare that they have no known competing financial interests or personal relationships that could have appeared to influence the work reported in this paper.

Acknowledgements

The financial support from the NSF MEP Program via Award No. 1763128 is gratefully acknowledged.

Appendix A. Measurement of the dihedral angles

The free energy landscape of a phase-separating alloy within the framework of a regular solution system is dependent on the interaction parameters [39]. From Young's equation (Eq. (35)), we may surmise that the dihedral angle is also dependent on the relative values of the interaction parameters, χ_{AB},χ_{Av}, and χ_{Bv}. However, we encounter a significant challenge in understanding the geometry that the dihedral angles impart to phases at the triple-point, due to the complex nature of the analytical equations that determine the excess energies at the surface and interphase boundaries. We, therefore, study grooving phenomenon in annealed films consisting of two equal-sized domains of pure A and B components in contact with the vapor until a steady state is reached. Simulations are performed in a large simulation domain of size 2000×400, which is divided equally into domains of pure A, B and vapor components, as shown in Fig. A.1. Grooving is promoted at the triple junction of the three phases by adjusting the interaction parameters, χ_{AB},χ_{Av} and χ_{Bv}, which in-turn modulate the excess energies at the interface between α and β phases, and the surface between film and vapor. No-flux boundary conditions are imposed along the two principal axes, and the films are allowed to anneal until grooves appear at the triple junction, for a maximum of 200,000 time-steps. The following values are assigned to the interaction parameters: $\chi_{AB} = 3.5$ (constant across all simulations), $\chi_{Av} = \chi_{Bv} = 2.7, 2.8$ and 3.5. Owing to the inherent geometry of the system at $\chi_{AB} = \chi_{Av} = \chi_{Bv} = 3.5$, we can ascertain that the theoretical dihedral angle for a film simulated with this condition should be equal to 120°. Using this as the baseline, we evaluate the dihedral angles for at the grooving locations for the above films using curve-fitting tools, as shown in Fig. A.1. The dihedral angle is extracted by tracing the angle between

the tangents to the fitted-curves at the triple-junction. The values are listed in Table 3.

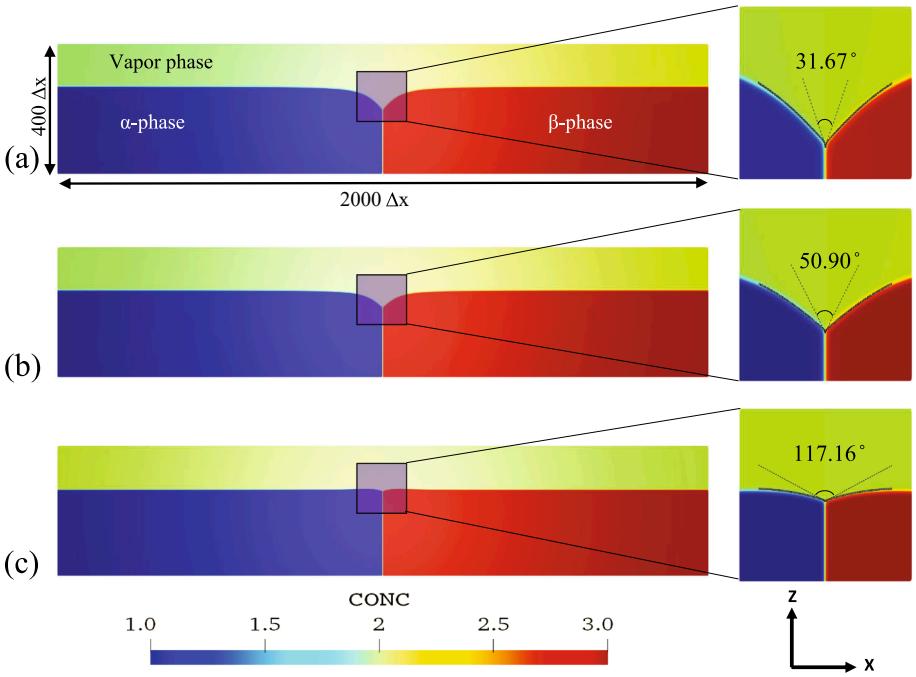

Fig. A.1. Simulations of a binary phase-separated film in contact with a vapor phase annealed to 200,000 time-steps, until grooves are formed at the triple-junction, shown on left. Dihedral angles are calculated between the tangents to curves fitted along the interfaces, as shown in the boxed regions on the right. Prescribed interaction parameters for each simulation are (a) $\chi_{Av} = \chi_{Bv} = 2.7$ and $\chi_{AB} = 3.5$, (b) $\chi_{Av} = \chi_{Bv} = 2.8, \chi_{AB} = 3.5$ and (c) $\chi_{AB} = \chi_{Av} = \chi_{Bv} = 3.5$.

References

[1] H. Guo, P.F. Yan, Y.B. Wang, J. Tan, Z.F. Zhang, M.L. Sui, E. Ma, Nat. Mater. 6 (2007) 735.
[2] O. Glushko, M. Mühlbacher, C. Gammer, M.J. Cordill, C. Mitterer, J. Eckert, Sci. Rep. 9 (2019) 1.
[3] M. Apreutesei, P. Steyer, L. Joly-Pottuz, A. Billard, J. Qiao, S. Cardinal, F. Sanchette, J.M. Pelletier, C. Esnouf, Thin Solid Films 561 (2014) 53.
[4] S.A. Harrington, J. Zhai, S. Denev, V. Gopalan, H. Wang, Z. Bi, S.A. Redfern, S. H. Baek, C.W. Bark, C.B. Eom, Q. Jia, M.E. Vickers, J.L. MacManus-Driscoll, Nat. Nanotechnol. 6 (2011) 491.
[5] J.L. MacManus-Driscoll, P. Zerrer, H. Wang, H. Yang, J. Yoon, A. Fouchet, R. Yu, M. G. Blamire, Q. Jia, Nat. Mater. 7 (2008) 314.
[6] Z. Chen, X. Wang, Y. Qi, S. Yang, J.A. Soares, B.A. Apgar, R. Gao, R. Xu, Y. Lee, X. Zhang, J. Yao, L.W. Martin, ACS Nano 10 (2016) 10237.
[7] L. Li, L. Sun, J.S. Gomez-Diaz, N.L. Hogan, P. Lu, F. Khatkhatay, W. Zhang, J. Jian, J. Huang, Q. Su, M. Fan, C. Jacob, J. Li, X. Zhang, Q. Jia, M. Sheldon, A. Al'u, X. Li, H. Wang, Nano Lett. 16, 3936 (2016).
[8] G. Chen, T. Wang, G. Stringfellow, Appl. Phys. Lett. 56 (1990) 1.
[9] A.G. Norman, T.Y. Seong, I.T. Ferguson, G.R. Booker, B.A. Joyce, Semicond. Sci. Technol. 8 (1993) S9.
[10] T.Y. Seong, A.G. Norman, I.T. Ferguson, G.R. Booker, J. Appl. Phys. 73 (1993) 8227.
[11] S.P. Ahrenkiel, S.H. Xin, P.M. Reimer, J.J. Berry, H. Luo, S. Short, M. Bode, M. Al-Jassim, J.R. Buschert, J.K. Furdyna, Phys. Rev. Lett. 75 (1995) 1586.
[12] C.Q. Chen, Y.T. Pei, K.P. Shaha, J.T.M. De Hosson, Appl. Phys. Lett. 96 (2010).
[13] F. Peiro, A. Cornet, J.R. Morante, A. Georgakilas, C. Wood, A. Christou, Appl. Phys. Lett. 66 (1995) 2391.
[14] S.W. Jun, T.Y. Seong, J.H. Lee, B. Lee, Appl. Phys. Lett. 68 (1996) 3443.
[15] V. Fink, E. Chevalier, O.J. Pitts, M.W. Dvorak, K.L. Kavanagh, C.R. Bolognesi, S. P. Watkins, S. Hummel, N. Moll, Appl. Phys. Lett. 79 (2001) 2384.
[16] S. Francoeur, M.C. Hanna, A.G. Norman, A. Mascarenhas, Appl. Phys. Lett. 80 (2002) 243.
[17] T. Seppänen, P.O.Å. Persson, L. Hultman, J. Birch, G.Z. Radnóczi, J. Appl. Phys. 97 (2005), 083503.
[18] J.R. Bortoleto, H.R. Gutírrez, M.A. Cotta, J. Bettini, Appl. Phys. Lett. 87 (2005) 1.
[19] N.A. El-Masry, E.L. Piner, S.X. Liu, S.M. Bedair, Appl. Phys. Lett. 72 (1998) 40.
[20] T.Y. Seong, I.T. Bae, C.J. Choi, D.Y. Noh, Y. Zhao, C.W. Tu, J. Appl. Phys. 85 (1999) 3192.
[21] K. Ankit, B. Derby, R. Raghavan, A. Misra, M.J. Demkowicz, J. Appl. Phys. 126 (2019), https://doi.org/10.1063/1.5110410.
[22] K. Fukutani, Y. Ishida, K. Tanji, T. Den, Thin Solid Films 515 (2007) 4629.
[23] K. Fukutani, K. Tanji, T. Saito, T. Den, Jpn. J. Appl. Phys. 47 (2008) 1140.
[24] R. Raghavan, A. Mukherjee, K. Ankit, J. Appl. Phys. 128 (2020), 175303.
[25] E.D. Tober, R.F.C. Farrow, R.F. Marks, G. Witte, K. Kalki, D.D. Chambliss, Phys. Rev. Lett. 81 (1998) 1897.
[26] R. Banerjee, A. Puthucode, S. Bose, P. Ayyub, Appl. Phys. Lett. 90 (2007) 21904.
[27] B. Derby, Y. Cui, J. Baldwin, A. Misra, Thin Solid Films 647 (2018) 50.
[28] F.T.N. Vüllers, R. Spolenak, Acta Mater. 99 (2015) 213.
[29] B.A. Movchan, A.V. Demchishin, Fiz. Met. Met. 28 (1969).
[30] D.P. Tracy, D.B. Knorr, J. Electron. Mater. 22 (1993) 611.
[31] J.A. Thornton, J. Vac. Sci. Technol. 12 (1975) 830.
[32] N. Saunders, A.P. Miodownik, J. Mater. Sci. 22 (1987) 629.
[33] M. Atzmon, D.A. Kessler, D.J. Srolovitzc, J. Appl. Phys. 72 (2) (1992) 442.
[34] C. Adams, D. Srolovitz, M. Atzmon, J. Appl. Phys. 74 (1993) 1707.
[35] Y. Lu, C. Wang, Y. Gao, R. Shi, X. Liu, Y. Wang, Phys. Rev. Lett. 109 (2012) 1.
[36] R. Raghavan, P.-E. Chen, Y. Jiao, K. Ankit, J. Appl. Phys. 129 (2021), 245301.
[37] L.T. Mushongera, M. Fleck, J. Kundin, Y. Wang, H. Emmerich, Acta Mater. 93 (2015) 60.
[38] L.T. Mushongera, M. Fleck, J. Kundin, F. Querfurth, H. Emmerich, Adv. Eng. Mater. 17 (2015) 1149.
[39] J.W. Cahn, J.E. Hilliard, J. Chem. Phys. 28 (1958) 258, arXiv:9809069v1 arXiv:gr-qc.
[40] M. Fleck, L. Mushongera, D. Pilipenko, K. Ankit, H. Emmerich, Eur. Phys. J. Plus 126 (2011) 95.
[41] H. Ramanarayan, T.A. Abinandanan, Acta Mater. 51 (2003) 4761.
[42] H. Ramanarayan, T.A. Abinandanan, Acta Mater. 52 (2004) 921.
[43] J.E. Morral, J.W. Cahn, Acta Metall. 19 (1971) 1037.
[44] L.Q. Chen, Acta Metall. Mater. 42 (1994) 3503.
[45] E.J. Kramer, P. Green, C.J. Palmstrøm, Polymer (Guildf) 25 (1984) 473.
[46] C. Huang, M.O. de la Cruz, B.W. Swift, Macromolecules 28 (1995) 7996.
[47] S. Bhattacharyya, T.A. Abinandanan, Bull. Mater. Sci. 26 (2003) 193.
[48] S. Sugathan, S. Bhattacharya, Comput. Mater. Sci. 172 (2020), 109284.
[49] D.A. Cogswell, A phase-field study of ternary multiphase microstructures, Ph.D. thesis, Massachusetts Institute of Technology (2010).
[50] M. Powers, B. Derby, E. Raeker, N. Champion, A. Misra, Thin Solid Films 693 (2020), 137692.
[51] S.Y. Hu, L.Q. Chen, Acta Mater. 49 (2001) 1879.
[52] B.K. Derby, A. Chatterjee, A. Misra, J. Appl. Phys. 128 (2020), https://doi.org/10.1063/5.0014441.
[53] B. Derby, Y. Cui, J. Baldwin, R. Arróyave, M.J. Demkowicz, A. Misra, Mater. Res. Lett. 7 (2019) 1.